A&A 420, 423–435 (2004)
DOI: 10.1051/0004-6361:20040992

Astronomy & Astrophysics

The structure of radiative shock waves

V. Hydrogen emission lines

Y. A. Fadeyev[1] and D. Gillet[2]

[1] Institute for Astronomy of the Russian Academy of Sciences, Pyatnitskaya 48, 119017 Moscow, Russia
[2] Observatoire de Haute-Provence – CNRS, 04870 Saint–Michel l'Observatoire, France

Received 8 January 2004 / Accepted 11 March 2004

Abstract. We considered the structure of steady-state plane-parallel radiative shock waves propagating through the partially ionized hydrogen gas of temperature $T_1 = 3000$ K and density 10^{-12} g cm^{-3} $\le \rho_1 \le 10^{-9}$ g cm^{-3}. The upstream Mach numbers range within $6 \le M_1 \le 14$. In frequency intervals of hydrogen lines the radiation field was treated using the transfer equation in the frame of the observer for the moving medium, whereas the continuum radiation was calculated for the static medium. Doppler shifts in Balmer emission lines of the radiation flux emerging from the upstream boundary of the shock wave model were found to be roughly one-third of the shock wave velocity: $-\delta V \approx \frac{1}{3}U_1$. The gas emitting the Balmer line radiation is located at the rear of the shock wave in the hydrogen recombination zone where the gas flow velocity in the frame of the observer is approximately one-half of the shock wave velocity: $-V^* \approx \frac{1}{2}U_1$. The ratio of the Doppler shift to the gas flow velocity of $\delta V/V^* \approx 0.7$ results both from the small optical thickness of the shock wave in line frequencies and the anisotropy of the radiation field typical for the slab geometry. In the ambient gas with density of $\rho_1 \gtrsim 10^{-11}$ g cm^{-3} the flux in the Hα frequency interval reveals the double structure of the profile. A weaker Hβ profile doubling was found for $\rho_1 \gtrsim 10^{-10}$ g cm^{-3} and $U_1 \lesssim 50$ km s^{-1}. The unshifted redward component of the double profile is due to photodeexcitation accompanying the rapid growth of collisional ionization in the narrow layer in front of the discontinuous jump.

Key words. shock waves – hydrodynamics – radiative transfer – stellar atmospheres – line: profiles

1. Introduction

It is now a well-established fact that hydrogen emission lines are a characteristic feature of radially pulsating stars of various types. Strong hydrogen emission is observed in Mira type (Joy 1947, 1954), W Vir (Abt 1954; Wallerstein 1959) and RV Tau (Preston 1962) pulsating variables. Moreover, in the spectra of Mira stars Balmer emission lines persist during the major part of the pulsation period (Joy 1947; Richter & Wood 2001). The intensity of the hydrogen emission seems to correlate with the amplitude of the pulsation since RR Lyr variables exhibit only weak emission lines (Preston 1964) and in classical Cepheids (for example in β Dor) hydrogen emission lines are scarcely detected (Hutchinson et al. 1975). The hydrogen emission in the spectra of pulsating stars is thought to be due to radiative cooling of the gas compressed by the shock wave propagating through the stellar atmosphere in each pulsation cycle (Kraft et al. 1959; Wallerstein 1959; Abt & Hardie 1960; Gorbatskii 1961).

High resolution spectroscopy reveals the doubling of Hα and Hβ emission profiles, whereas profiles of higher Balmer lines exhibit only the asymmetry. This feature is observed not only in Mira stars (Bidelman & Ratcliffe 1954; Fox et al. 1984; Gillet 1988; Woodsworth 1995) but also in W Vir and RV Tau variables (Lèbre & Gillet 1991, 1992). Bidelman & Ratcliffe (1954) explained the Hα profile doubling observed in the Mira type star T Cen as an absorption reversal rather than a real duplicity, the absorption resulting from the cool hydrogen gas above the propagating shock wave. Willson (1976) interpreted the double structure of the emission profiles in terms of a spherically symmetric shock wave with a radial distance from the center of the star appreciably larger than the radius of the photosphere. According to this model the flux of the redshifted component emerges from the back side of the shock wave moving outward from the observer. Woodsworth (1995) modelled double Hα profiles as three emission components of equal width, two of which are blended. Thus, different phenomenological models demonstrate the ambiguity existing so far in our understanding of the origin of the Balmer emission lines produced by the shock waves in stellar atmospheres.

This paper is the fifth in our series on the structure of radiative shock waves. In our previous Papers I–IV (Fadeyev & Gillet 1998, 2000, 2001; Fadeyev et al. 2002) we presented the method of computation and described results for the structure of radiative shock waves propagating through partially ionized hydrogen gas with temperature and density typical for atmospheres of pulsating late-type stars. An advantage of this

Send offprint requests to: D. Gillet, e-mail: gillet@obs-hp.fr

approach is that the gas dynamics, radiation field and atomic level populations are considered self-consistently for the whole shock wave model. However, in all our previous papers the radiative transfer was treated in a static medium approximation, so that we were unable to compare the calculated monochromatic radiation flux with observed emission profiles. Below we describe the shock wave models with Doppler shifts in the line profiles computed from the transfer equation in the frame of the observer.

2. Method of computation

As in our previous studies we consider a steady-state plane-parallel shock wave propagating through a homogeneous medium consisting solely of atomic hydrogen gas. The shock wave model is represented by a flat finite slab moving together with a discontinuous jump toward the observer at velocity V_s which is regarded as negative. The unperturbed gas enters the upstream face of the slab with velocity $U_1 = -V_s$, and throughout this paper U_1 is referred as the shock wave velocity.

The space coordinate X is measured along the path of the gas element moving through the slab and is within the range $X_1 \le X \le X_N$, where X_1 and X_N are the coordinates of the upstream and downstream faces of the slab, respectively. We set $X = 0$ at the discontinuous jump where the gas flow velocity U and the gas density ρ undergo an abrupt change. At the upstream face of the slab the gas is assumed to be unperturbed, whereas at the downstream slab boundary the electron temperature T_e and the hydrogen ionization degree x_H are assumed to approach their postshock asymptotic values. In general, the space coordinates of both boundaries were determined from trial calculations in such a way that the solution describing the structure of the shock wave is independent of coordinates X_1 and X_N.

For the calculation of the shock wave structure we follow our previos studies (Papers I and II) and solve the initial value problem for the fluid dynamics and rate equations treated as a system of ordinary differential equations, while radiative transfer is treated as a two-point boundary value problem. To take into account the strong coupling between the gas flow and the radiation field produced by this flow the ordinary differential equations and the transfer equation are solved iteratively.

The radiation transfer equation is solved with the improved Feautrier method (Rybicki & Hummer 1991) and the slab is divided into $N = 1.6 \times 10^4$ cells with 6000 cells ahead of the discontinuous jump. Space intervals $\Delta X_{j-1/2} = X_j - X_{j-1}$ increase in a geometrical progression in both directions from the cell interface $X_{\mathcal{J}} = 0$. For the sake of convenience the variables at the cell centers nearest to the discontinuous jump are denoted with superscripts minus and plus, that is $X^- = X_{\mathcal{J}-1/2}$ and $X^+ = X_{\mathcal{J}+1/2}$.

The frequency range 7×10^{13} Hz $\le \nu \le 10^{16}$ Hz consists of a set of intervals with boundaries either at hydrogen ionization thresholds or at limits of line frequency intervals. In the present study we consider the hydrogen atom with $L = 5$ bound levels and the continuum, so that the full frequency range is represented by 15 intervals for the continuum and by 10 intervals for lines.

The electron collision excitation rates were calculated with effective collision strengths from Scholz et al. (1990) for the $1 \to 2$ transition, from Callaway (1994) for the $1 \to 3$ and $2 \to 3$ transitions and from Aggarwal et al. (1991) for other bound-bound transitions. The electron collision ionization rates were computed with polynomial fits from Lennon et al. (1986). The photoexcitation rates were calculated for Doppler profiles.

In general, the interaction of the radiation field with the moving medium is described in terms of the comoving frame partial differential transfer equation. The method developed by Mihalas et al. (1975) treats the comoving frame transfer equation as a two-point boundary value problem with respect to the spatial coordinate and as a Cauchy problem with respect to the frequency. However our attempts to apply such an approach to the shock wave structure failed due to numerical instability arising because of the existence of the velocity jump. The difficulties accompanying the solution of the comoving frame transfer equation for nonmonotonic gas flow velocity fields were discussed earlier by Mihalas (1980).

In our study the ratio of the gas flow velocity to the speed of light is confined to values of $U/c \lesssim 3 \times 10^{-4}$, so that the only significant effect of the moving medium is the Doppler shift in the spectral lines. The radiation flux within all line frequency intervals is less than $\sim 10^{-3}$ of the total radiative flux produced by the shock wave, so that we assume that without significant loss of self-consistency the Doppler shifts can be regarded as insignificant for the structure of the shock wave. Such an assumption allowed us to calculate the shock wave model iteratively with a static transfer equation. When the iteration procedure converges, we solve the transfer equation in line frequency intervals for the moving medium. In support of this approach below we compare solutions of the transfer equation for a moving and for a static medium.

In plane parallel geometry the transfer equation in the frame of the observer is (Mihalas 1978)

$$\mu \frac{\mathrm{d}I_\nu(\mu)}{\mathrm{d}X} = \eta_\nu(\mu) - \chi_\nu(\mu) I_\nu(\mu), \tag{1}$$

where $\mu = \cos(\theta)$ is the directional cosine, $I_\nu(\mu)$ is the specific intensity, $\eta_\nu(\mu)$ and $\chi_\nu(\mu)$ are the emission and extinction coefficients, respectively. For brevity in Eq. (1) we omit the functional dependencies on X.

The motion toward the observer is regarded as negative, whereas the velocity in the frame of the shock U is positive. Velocities in both frames relate via

$$\begin{aligned} V &= V^- + U^- - U, \quad (X < 0), \\ V &= V^+ + U^+ - U, \quad (X > 0), \end{aligned} \tag{2}$$

where $V^- = U^- - U_1$ and $V^+ = U^+ - U_1$. Thus, the postshock compression ratio expressed in terms of the gas flow velocity in the frame of the observer is given by

$$\frac{\rho}{\rho_1} = \frac{V_s}{V_s - 2V^+ + V}. \tag{3}$$

Though on the r.h.s. of Eq. (3) we have only the observer's frame velocity, this expression is equivalent to Eq. (8) given in Paper III where the postshock compression ratio is expressed in

terms of the specific internal energy of the gas and the radiation flux.

The line opacity and line emissivity coefficients $\kappa_\nu^\ell(\mu)$ and $\eta_\nu^\ell(\mu)$ are calculated on the assumption of complete redistribution, with the Doppler profile given by

$$\phi(\nu) = \frac{1}{\Delta\nu_\mathrm{D}\sqrt{\pi}} \exp\left[-\left(\nu - \nu_0 + \frac{\nu_0}{c}\mu V\right)^2 / \Delta\nu_\mathrm{D}^2\right], \quad (4)$$

where ν_0 is the line-center frequency,

$$\Delta\nu_\mathrm{D} = \frac{\nu_0}{c}\left(\frac{2kT_\mathrm{a}}{m_\mathrm{H}}\right)^{1/2} \quad (5)$$

is the Doppler width, and m_H is the mass of hydrogen atom.

3. Shock wave model

The self-consistent solution of the equations of fluid dynamics, radiative transfer and rate equations for atomic level populations describes the structure of the shock wave and depends on three general parameters, which are: the density ρ_1 and the temperature T_1 of the unperturbed gas, and the velocity of the shock wave U_1 with respect to the ambient gas. The structure of the radiative shock wave is shown in Fig. 1 where the following are plotted as a function of space coordinate X: the electron temperature T_e and the temperature of hydrogen atoms T_a (here we assume that neutral hydrogen atoms and hydrogen ions have the same temperature), the hydrogen ionization degree x_H, the total radiative flux F_R, and the Lyman continuum flux F_Ly. For the sake of convenience we use a logarithmic scale with respect to the space coordinate, so that each variable is represented by two separate plots for the preshock ($X < 0$) and postshock ($X > 0$) regions, respectively.

In the partially ionized hydrogen gas the upstream boundary of the shock wave is associated with ionization of hydrogen atoms ahead of the discontinuous jump, whereas the downstream boundary is associated with the recombination zone. Within the major part of the plots shown in the lower panel of Fig. 1 the total radiative flux is upstream (i.e. $F_\mathrm{R} < 0$) since the radiation is generated at the rear of the shock wave in the hydrogen recombination zone. The total radiative fluxes emerging from both faces of the slab in opposite directions are nearly equal, that is, $-F_\mathrm{R1} \approx F_\mathrm{RN}$.

The interaction of the gas flow with the radiative field due to absorption or emission of radiation is described in terms of the divergence of the total radiative flux

$$\nabla \cdot F_\mathrm{R} = 4\pi \int_0^\infty (\eta_\nu - \kappa_\nu J_\nu)\,\mathrm{d}\nu, \quad (6)$$

where J_ν is the mean intensity. In the upper panel of Fig. 2 we show the plots of $\nabla \cdot F_\mathrm{R}$ computed for the moving and for the static medium. In the preshock region (-10^4 cm $\lesssim X < 0$ cm) the gas is radiatively heated due to absorption of the Lyman continuum radiation. Just ahead of the discontinuous jump (-10^2 cm $\lesssim X < 0$ cm) radiative heating substantially increases because of absorption of radiation in Lyman lines though at Balmer frequencies the gas emits more energy than it absorbs.

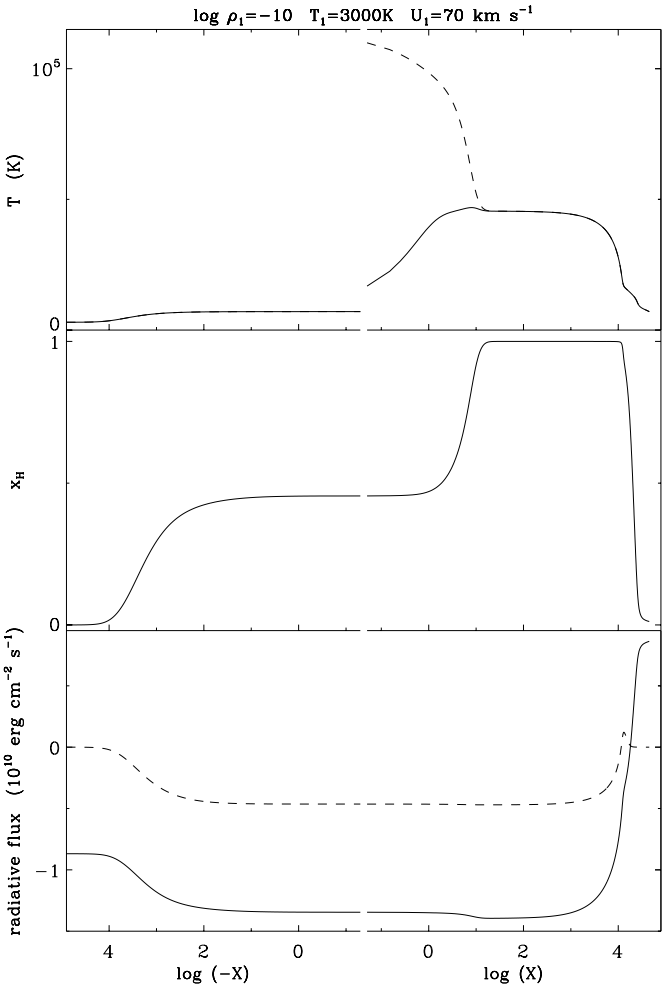

Fig. 1. The structure of the radiative shock wave. The left- and right-hand sides of the plots represent the preshock and postshock regions, respectively. *Upper panel*: the electron temperature T_e (solid line) and the temperature of neutral hydrogen atoms and hydrogen ions T_a (dashed line). *Middle panel*: the hydrogen ionization degree x_H. *Lower panel*: the total radiative flux F_R (solid line) and the Lyman continuum flux F_Ly (dashed line). The space coordinate X is in centimeters.

The radiative cooling of the gas due to emission in Balmer lines is less by an order of magnitude than radiative heating due to absorption in Lyman lines.

Such a difference in behaviour of the radiation field in the Lα and Hα frequency intervals is clearly seen from the comparison of the plots of the divergence of the line radiation flux

$$\nabla \cdot F_\ell = 4\pi \int_{\nu_0-\Delta\nu}^{\nu_0+\Delta\nu} [\eta_\nu(\mu) - \kappa_\nu(\mu) J_\nu]\,\mathrm{d}\nu \quad (7)$$

shown in the middle and lower panels of Fig. 2. Here $\Delta\nu = 3.5\times10^{-4}\nu_0$ is the half-width of the line frequency interval. The opacity and emissivity coefficients are $\kappa_\nu(\mu) = \kappa_\nu^\ell(\mu) + \kappa_\nu^c$ and $\eta_\nu(\mu) = \eta_\nu^\ell(\mu) + \eta_\nu^c$, respectively, where superscripts ℓ and c denote the line and the continuum variables. Thus, expression (7) defines the divergence of the radiative flux for both line and continuum radiation. It should be noted, however, that the contribution of the continuum radiation can be neglected because

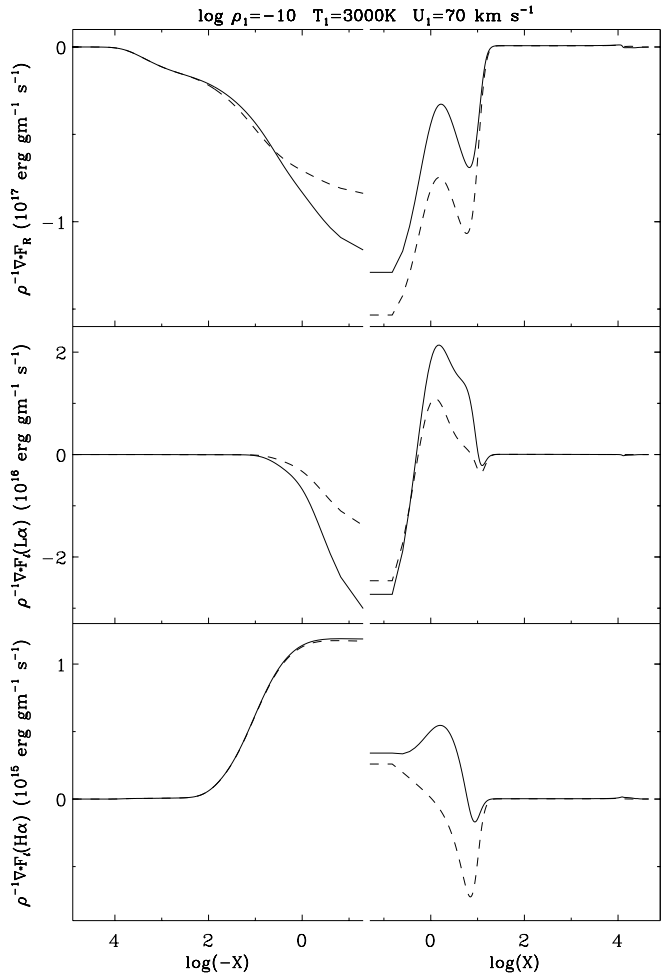

Fig. 2. The divergence of the total radiative flux (*upper panel*), of the Lα radiative flux (*middle panel*) and of the Hα radiative flux (*lower panel*) as a function of space coordinate X. Solid and dashed lines show the solutions for the moving and for the static medium, respectively.

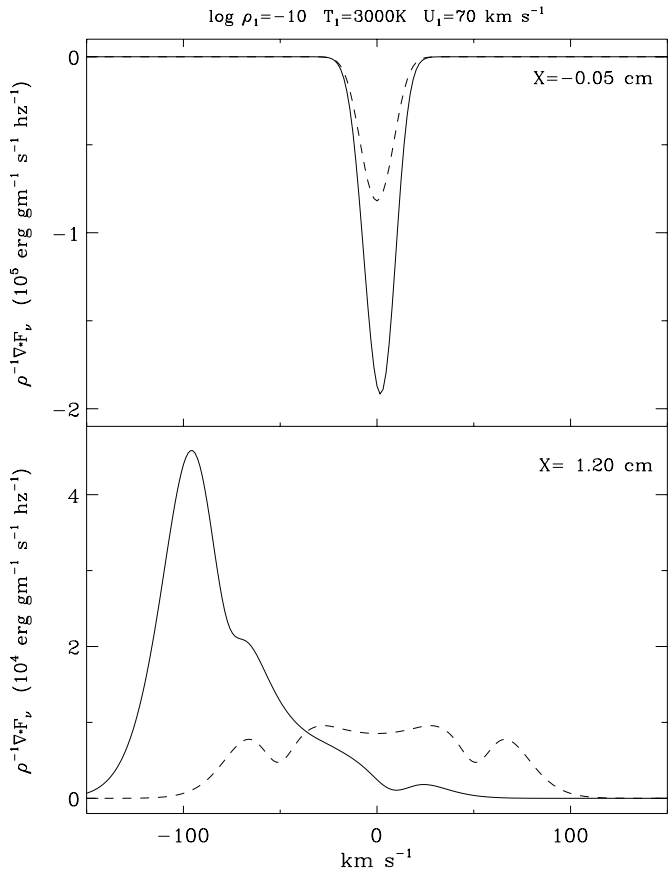

Fig. 3. The divergence of the monochromatic radiative flux within the Lα frequency interval just ahead of the discontinuous jump (*upper panel*) and at the maximum of $\nabla\cdot F_\ell(\mathrm{L}\alpha)$ (*lower panel*). Solid and dashed lines show the solutions for the moving and for the static medium, respectively.

the maximum values of the line opacity and line emissivity coefficients dominate the continuum values by as much as two orders of magnitude.

Most of the spectral line radiation is transported in Lyman series lines. As is seen in the middle panel of Fig. 2, Doppler shifts lead to stronger radiative heating of the gas ahead of the discontinuous jump and to stronger radiative cooling behind the discontinuous jump. However the size of this zone is about four orders of magnitude less than the length of the shock wave, so that the effects of Doppler shifts are small enough and can be neglected. For example, the change of the upstream Lα radiative flux due to Doppler shifts does not exceed 10%, whereas the Lα radiative flux emerging from the upstream face of the slab is less than 10^{-3} of the total radiative flux. For the model shown in Figs. 1 and 2 the optical thickness of the slab at Lα and Hα line-center frequencies is $\tau_0(\mathrm{L}\alpha)\approx 6\times10^6$ and $\tau_0(\mathrm{H}\alpha)\approx 40$, respectively.

Thus, the effects of Doppler shifts are most pronounced in the close vicinity of the discontinuous jump. In Fig. 3 we show the plots of the divergence of the monochromatic radiative flux $\nabla\cdot F_\nu(\mathrm{L}\alpha)$ as a function of frequency ν for the cell center X^- just ahead the discontinuous jump and for the maximum of $\nabla\cdot F_\ell(\mathrm{L}\alpha)$ behind the discontinuous jump (see the middle panel of Fig. 2.

4. Formation of line radiation

Within the shock wave one can delineate three distinct zones with substantial changes of level populations n_i due to radiative bound-bound transitions that lead to the appreciable emission of spectral line radiation. To compare the effect that different atomic transitions have on the line radiation in transition $i\to j$ we calculate the net photoexcitation rates

$$Z_{ij} = n_i R_{ij} - n_j \frac{n_i^*}{n_j^*} R_{ij}^\dagger \tag{8}$$

and the net collisional excitation rates

$$Y_{ij} = n_\mathrm{e} C_{ij}\left[n_i - n_j\left(n_i^*/n_j^*\right)\right], \tag{9}$$

where R_{ij} and $(n_i^*/n_j^*)R_{ij}^\dagger$ are the photoexcitation and photodeexcitation rates, respectively, C_{ij} is the rate of collisional excitation and n_i^*/n_j^* is the thermodynamic equilibrium ratio given by the Saha-Boltzmann relation for a nonequilibrium number

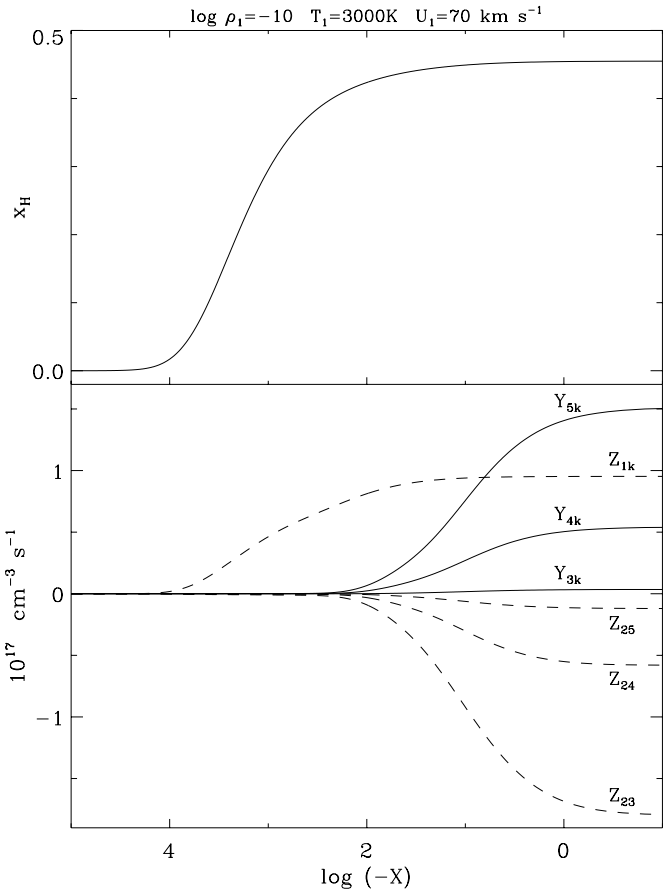

Fig. 4. The zone of the radiative precursor. *Upper panel*: the hydrogen ionization degree. *Lower panel*: net collisional ionization rates (solid lines) and net photoionization and photoexcitation rates (dashed lines).

density of electrons n_e. We also estimate the net photoionization rates

$$Z_{ik} = n_i R_{ik} - n_e \frac{n_i^*}{n_e^*} R_{ik}^{\dagger}, \tag{10}$$

where R_{ik} and $(n_i^*/n_e^*)R_{ik}^{\dagger}$ are the photoionization and photorecombination rates, respectively, and the net collisional ionization rates

$$Y_{ik} = n_i n_e C_{ik} \left(1 - \frac{n_e}{n_i}\frac{n_i^*}{n_e^*}\right), \tag{11}$$

where C_{ik} is the collisional ionization rate.

4.1. The radiative precursor

As can be seen in Fig. 4 the only essential atomic transition within the major part of the radiative precursor is photoionization from the ground state which is due to the absorption of the Lyman continuum radiation. However in the close vicinity of the discontinuous jump (-10^2 cm $\lesssim X \leq 0$) the rapid growth of collisional ionizations is accompanied by photodeexcitation while the rates of collisional bound-bound transitions remain negligible. The effect of preshock photodeexcitation on the structure of the shock wave is quite small; however, as we show below, they lead to remarkable features in the Hα and Hβ profiles of the emergent radiation flux.

To estimate the contribution of preshock photodeexcitations $3 \to 2$ on the emergent Hα radiation flux

$$F_\ell(\mathrm{H}\alpha) = \int_{\nu_0(\mathrm{H}\alpha)-\Delta\nu}^{\nu_0(\mathrm{H}\alpha)+\Delta\nu} F_\nu \mathrm{d}\nu \tag{12}$$

we calculated the quantity

$$\mathcal{F}(\mathrm{H}\alpha) = -\int_{X_1}^{0} \nabla \cdot F_\ell(\mathrm{H}\alpha)\mathrm{d}X. \tag{13}$$

The ratio $\mathcal{F}(\mathrm{H}\alpha)/F_\ell(\mathrm{H}\alpha)$ was found to decrease with decreasing gas density ρ_1. For example, in shock waves with velocity $U_1 \approx 70$ km s^{-1} the fraction of the preshock Hα emission in the emergent radiation flux $F_\ell(\mathrm{H}\alpha)$ is within the range $10^{-2} \lesssim \mathcal{F}(\mathrm{H}\alpha)/F_\ell(\mathrm{H}\alpha) \lesssim 0.2$ for 10^{-12} g cm$^{-3} \leq \rho_1 \leq 10^{-9}$ g cm^{-3}.

4.2. The zone of hydrogen ionization

Hydrogen ionization behind the discontinuous jump proceeds collisionally since photoionization rates are much lower than the rapidly increasing collisional ionization rates (see panel b in Fig. 5). The continuum radiation flux remains nearly constant so that any changes of the total radiation flux behind the discontinuous jump result mainly from Lα emission. In panel c in Fig. 5 we show the net collisional and photoexcitation rates for transitions 1−2 and 1−3. Even though photodeexcitation $2 \to 1$ does not exactly balance collisional excitation $1 \to 2$, it is responsible for strong emission of Lα photons and leads to appreciable radiative cooling of the gas seen in the middle panel in Fig. 2 as the maximum of $\nabla \cdot F_\ell(\mathrm{L}\alpha)$. Bound-bound transitions from the ground state to levels $j \geq 3$ are collisionally dominated and emission of radiation due to photodeexcitation is quite small. Among excitations from levels $i > 2$ one should only note the collisional transition $2 \to 3$ accompanied by emission of Hα photons (see panel d in Fig. 5), which however is scarcely perceptible.

4.3. The zone of hydrogen recombination

The center of the radiation emitting zone we define as a layer where the total radiative flux over the upstream hemisphere ($-1 \leq \mu \leq 0$) equals the total radiative flux over the downstream hemisphere ($0 \leq \mu \leq 1$), that is,

$$-\int_0^{\infty}\int_{-1}^{0} I_\nu(\mu)\mu \mathrm{d}\mu\mathrm{d}\nu = \int_0^{\infty}\int_{0}^{1} I_\nu(\mu)\mu \mathrm{d}\mu\mathrm{d}\nu. \tag{14}$$

Thus, in the center of the radiation emitting zone we have $F_R = 0$. For the model shown in Fig. 1 condition (14) is fulfilled in the hydrogen recombination zone at $x_H = 0.69$. It should be noted, however, that for the monochromatic radiation flux F_ν the space coordinate $X(F_\nu = 0)$ is frequency dependent. For example, the radiative flux averaged over the Lyman continuum changes its sign closer to the discontinuous jump in layers with $x_H \approx 0.99$.

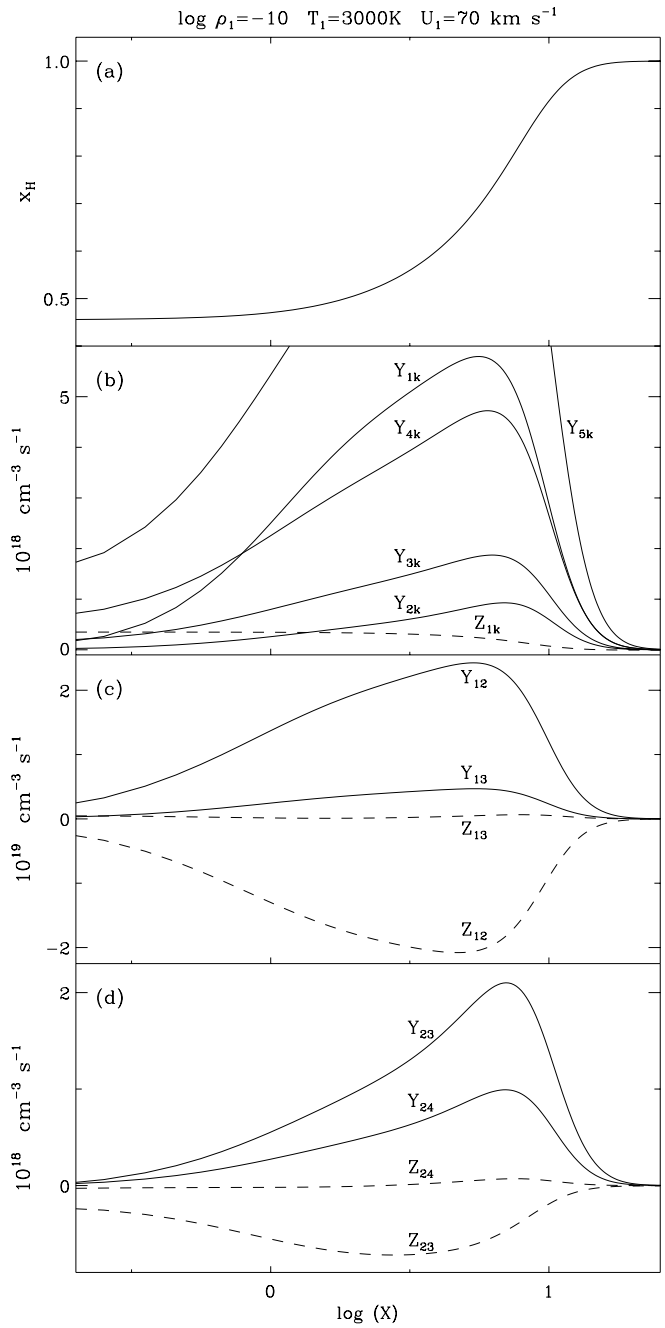

Fig. 5. The zone of hydrogen ionization behind the discontinuous jump. **a)** The hydrogen ionization degree. **b)** Net collisional ionization rates (solid lines) and the net photoionization rate Z_{1k} (dashed line). **c)**, **d)** Net collisional excitation rates (solid lines) and net photoexcitation rates (dashed lines).

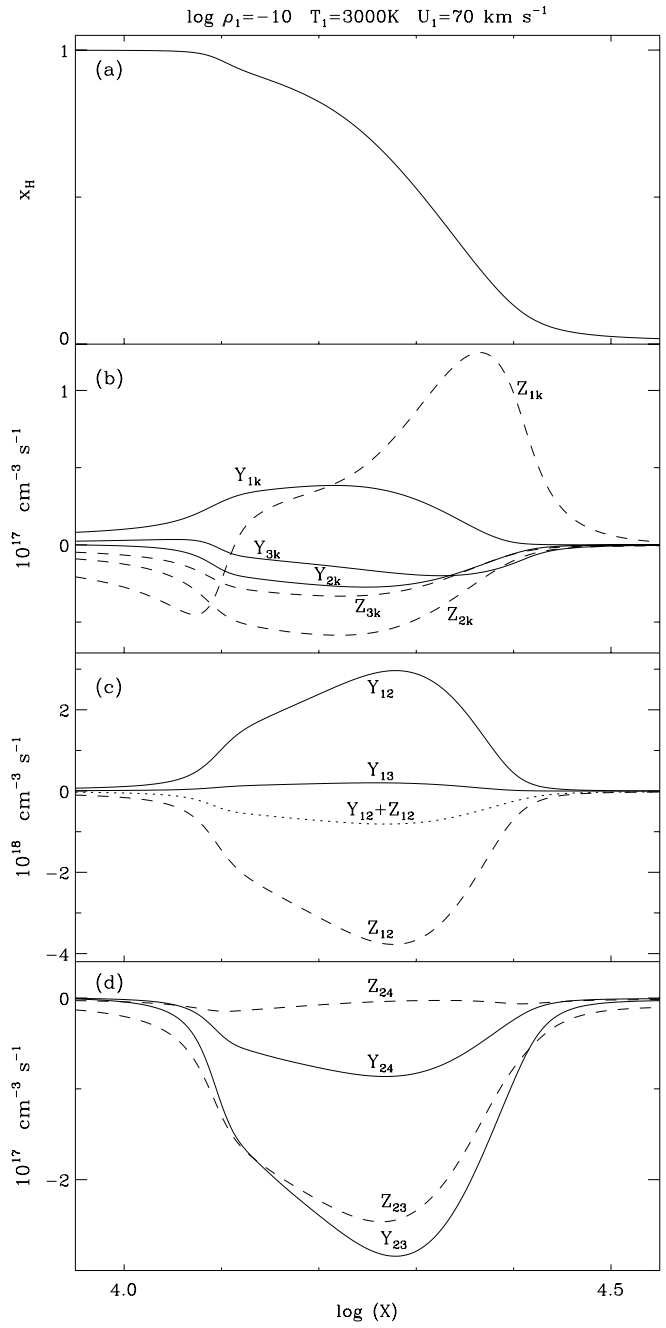

Fig. 6. The zone of hydrogen recombination at the rear of the shock wave. **a)** The hydrogen ionization degree. **b)** Net collisional ionization rates (solid lines) and net photoionization rates (dashed lines). **c)**, **d)** Net collisional excitation rates (solid lines) and net photoexcitation rates (dashed lines).

As is seen in panel b in Fig. 6, the initial hydrogen recombination results from radiative downward transitions to the ground state. However, at ionization degrees $x_H < 0.94$ recombination of hydrogen atoms is due to downward bound-free transitions on levels $i \geq 2$, both radiative and collisional, while atoms in the ground state undergo ionization. Thus, the final relaxation of the postshock gas is appreciably slowed down by ionization of the ground state hydrogen atoms.

In the recombination zone the ground-state hydrogen atoms undergo collisional excitation, though radiative bound-bound transitions have the opposite direction. Within the recombination zone the most conspicuous transition is excitation $1 \rightarrow 2$ which is accompanied by photodeexcitation $2 \rightarrow 1$ with resulting rate $Y_{12} + Z_{12} < 0$ (see panel c in Fig. 6). Though in the hydrogen recombination zone the absolute value of the net rate Z_{12} is about an order of magnitude less than in the ionization zone (compare plots in panel c in Fig. 6 with those in panel c in Fig. 5), most Lα photons of the shock wave are created in the recombination zone because of its much larger length. Collisional excitation $1 \rightarrow j$ for $j \geq 3$ is not

completely balanced by photodeexcitation, and the resulting transition rates are positive, that is, $Y_{1j} + Z_{1j} > 0$.

Populations of levels $i \geq 3$ undergo both collisional and radiative deexcitation. The net rates for transitions 2−3 and 2−4 are shown in panel d in Fig. 6. Thus, the formation of the Balmer line radiation takes place at the rear of the shock wave in the hydrogen recombination zone in layers around the minimum of $Z_{2j} < 0$. For the model shown in Fig. 6 the condition $F_\ell(\mathrm{H}\alpha) = 0$ corresponds to a hydrogen ionization degree of $x_\mathrm{H} \approx 0.87$, whereas for H$\beta$ and Hγ frequency intervals the condition of zero flux is fulfilled at $x_\mathrm{H} \approx 0.74$.

Transfer of the Balmer line radiation in the shock wave is illustrated in Fig. 7 where the monochromatic radiation flux F_ν in Hα, Hβ and Hγ frequency intervals is shown in three-dimensional plots as a function of spatial coordinate X and frequency ν. The plots are given on a linear scale with respect to X and for the sake of convenience we discarded the outermost preshock zones where the flux F_ν is almost independent of X. The frequency dependence of the flux is expressed in km s^{-1} with negative values corresponding to the blue shifts. The Balmer line-center flux is about two orders of magnitude greater than the continuum flux, so that the dependence of the continuum flux on the spatial coordinate X is not seen in these plots. According to notations adopted the upstream flux is negative. The frequency dependence of the space coordinate of the zero monochromatic flux $X(F_\nu = 0)$ is shown by thick contour lines.

5. The emergent flux at Balmer line frequencies

Of most interest for a comparison with the observations is the spectral line monochromatic radiation flux $F_{\nu 1}$ emerging from the upstream face of the shock wave model. In Fig. 8 we show the plots of $F_{\nu 1}$ as a function of frequency ν for Hα, Hβ and Hγ intervals. For the sake of convenience the flux is normalized with respect to the amplitude of the profile and is given with the opposite sign. It should be noted that in order to treat correctly the angular and frequency dependencies of the specific intensity $I_\nu(\mu)$, the line frequency intervals considered in our calculations were several times of those shown in Fig. 8.

The most conspicuous feature seen in Fig. 8 is an unshifted secondary maximum or a hump in the Hα and Hβ profiles. In the Hα frequency interval the hump is present at gas densities of $\rho_1 > 10^{-11}$ g cm^{-3} for all values of the shock wave velocity considered in our study (40 km s^{-1} $\leq U_1 \leq$ 90 km s^{-1}), while in the Hβ frequency interval the weak hump appears only at $\rho_1 > 10^{-10}$ g cm^{-3} and $U_1 < 60$ km s^{-1}. The hump becomes less prominent with decreasing gas density ρ_1 and at low densities is revealed as an asymmetry of the redward branch of the profile.

The hump in the Hα and Hβ flux profiles results from the radiation emitted by the narrow layer of the gas just ahead of the discontinuous jump. The contribution from the preshock gas is clearly seen when comparing the emergent flux profiles calculated for the moving and for the static medium. As is seen in Figs. 9 to 11, the frequency dependence of the emergent Hα flux for the static medium with $\rho_1 \gtrsim 10^{-10}$ g cm^{-3} can be represented as the superposition of the narrow and the broad emission profiles with origin in the preshock and postshock regions, respectively. The preshock emission nearly disappears for the line-center optical thickness of the shock wave of $\tau < 1$.

For $U_1 \gtrsim 70$ km s^{-1} the maximum of the preshock emission is blueshifted by one or a few km s^{-1}. This is due to the fact that the growth of the gas temperature in the gas element approaching the discontinuous jump is accompanied by an increase of the gas density ρ and, therefore, by a decrease of the gas flow velocity U. Thus, the preshock gas ahead of the discontinuous jump is slightly accelerated toward the observer and this effect is most conspicuous at higher densities due to stronger absorption of the Lyman continuum radiation. The Doppler shift of the redward emission component increases with increasing shock wave velocity U_1 (see plots for $\log \rho_1 = -9$ in Figs. 9 to 11) and for shock wave velocities within the range 70 km s^{-1} $\leq U_1 \leq$ 90 km s^{-1} the gas flow velocity in the frame of the observer just ahead of the discontinuous jump is 1 km s^{-1} $\leq -V^- \leq$ 3 km s^{-1}.

As was shown above, the preshock Balmer line emission zone is confined to the narrow layer ahead of the discontinuous jump where photodeexcitation rates rapidly increase while the gas element approaches the discontinuous jump (see the lower panel in Fig. 4). The hump in the flux profile disappears when the contribution of preshock radiative deexcitation becomes small in comparison with the line flux. For Hα line the condition of disappearance of the redward emission feature corresponds to $\mathcal{F}(\mathrm{H}\alpha)/F_\ell(\mathrm{H}\alpha) < 0.1$, where $\mathcal{F}(\mathrm{H}\alpha)$ is given by Eq. (13). The fraction of the preshock radiation in the line profile diminishes not only with decreasing gas density ρ_1 but also with increasing shock wave velocity U_1. In the latter case this is due to the increasing width of the profile accompanying the growth of the postshock temperature of heavy particles T_a^+.

To an accuracy of a few per cent the emergent line flux $F_\ell(\mathrm{H}\alpha)$ and the $FWHM$ of the line profile are the same for the moving and for the static medium, respectively. Because of the presence of the unshifted emission feature in the profiles of the emergent Hα radiation flux any estimate of the Doppler shift δV becomes ambiguous. In the present paper we evaluated δV using the same procedure for all profiles both with unshifted emission component and without it. To this end we determined the Doppler shift of the profile δV as the frequency interval between the profile center at its half height and the line-center frequency ν_0. Thus, values of δV might be underestimated at gas densities of $\rho_1 \gtrsim 10^{-10}$ g cm^{-3} because of the presence of the unshifted redward component.

The parameters of the shock wave models are summarised in Table 1 where we give Doppler shifts δV, $FWHM$ line widths w and optical depths at line-center frequency τ for Hα, Hβ and Hγ frequency intervals. Gas flow velocities as well as Doppler shifts and line widths are expressed in units of km s^{-1}. In the first three columns of Table 1 are listed the unperturbed gas density ρ_1, the shock wave velocity U_1 and the upstream Mach number M_1. The difference of the gas flow velocities in the frame of the observer just ahead and just behind the discontinuous jump $V^- - V^+$ gives the amplitude of the discontinuity. The columns labelled V^* and V_∞ give the velocity in the frame of the observer for the Hα emitting layer and the limiting gas flow velocity corresponding to isothermal compression of the shocked gas. The two last columns list the values of the

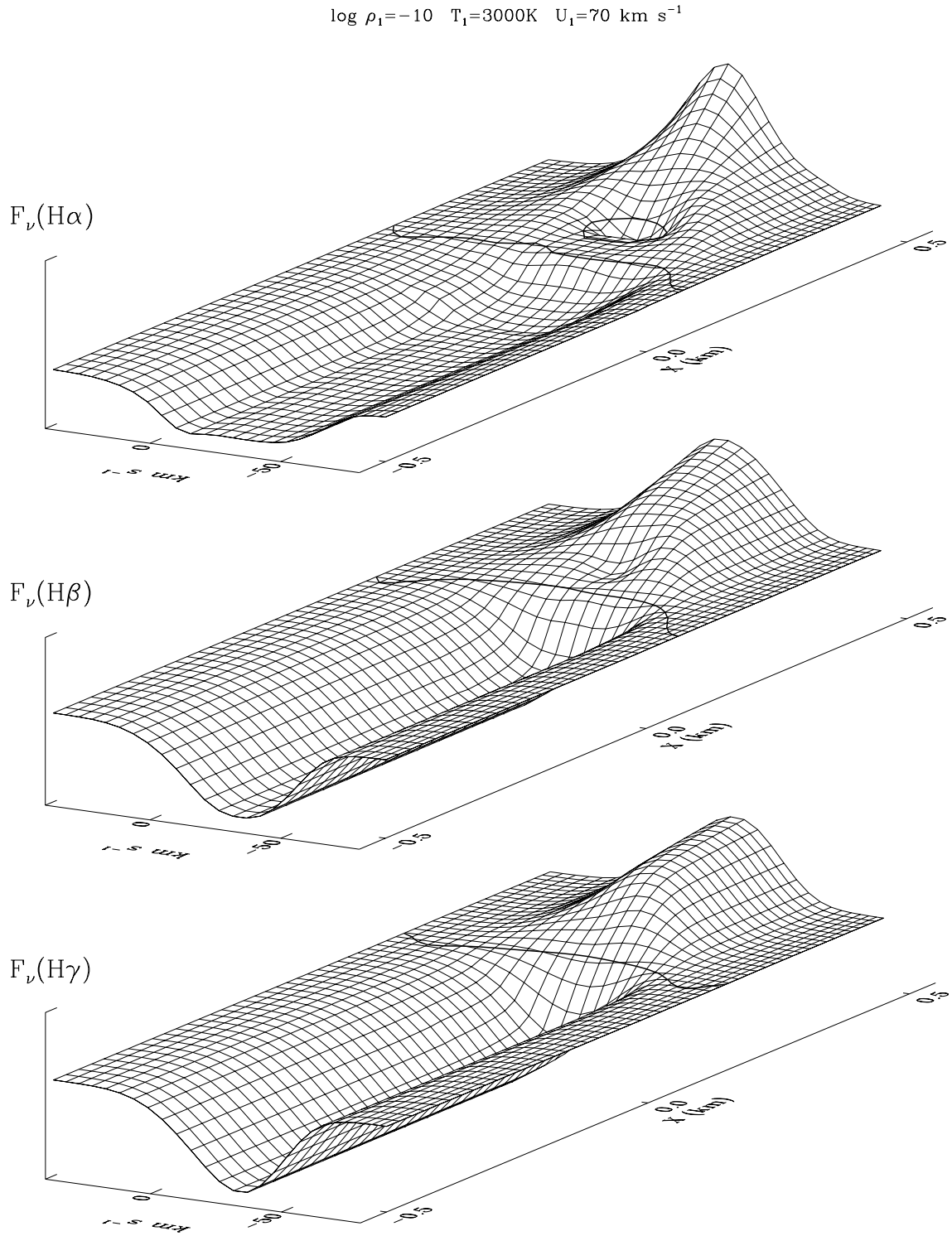

Fig. 7. The monochromatic flux F_ν in the frequency intervals of the Hα, Hβ and Hγ lines. Thick lines show the level of $F_\nu = 0$.

compression ratio at the Hα emitting layer $\eta^* = \rho^*/\rho_1$ and of the limiting isothermal compression ratio

$$\eta_\infty = \rho_\infty/\rho_1 = \gamma M_1^2, \tag{15}$$

where $\gamma = 5/3$ is the adiabatic exponent of the monoatomic gas.

Within the considered range of shock wave velocities 40 km s^{-1} $\le U_1 \le$ 90 (i.e. for Mach numbers ranging within $6.2 \le M_1 \le 14$) both Doppler shifts δV and $FWHM$ line widths w increase almost linearly with increasing shock wave velocity U_1. At the same time δV and w decrease with decreasing density of the unperturbed gas ρ_1.

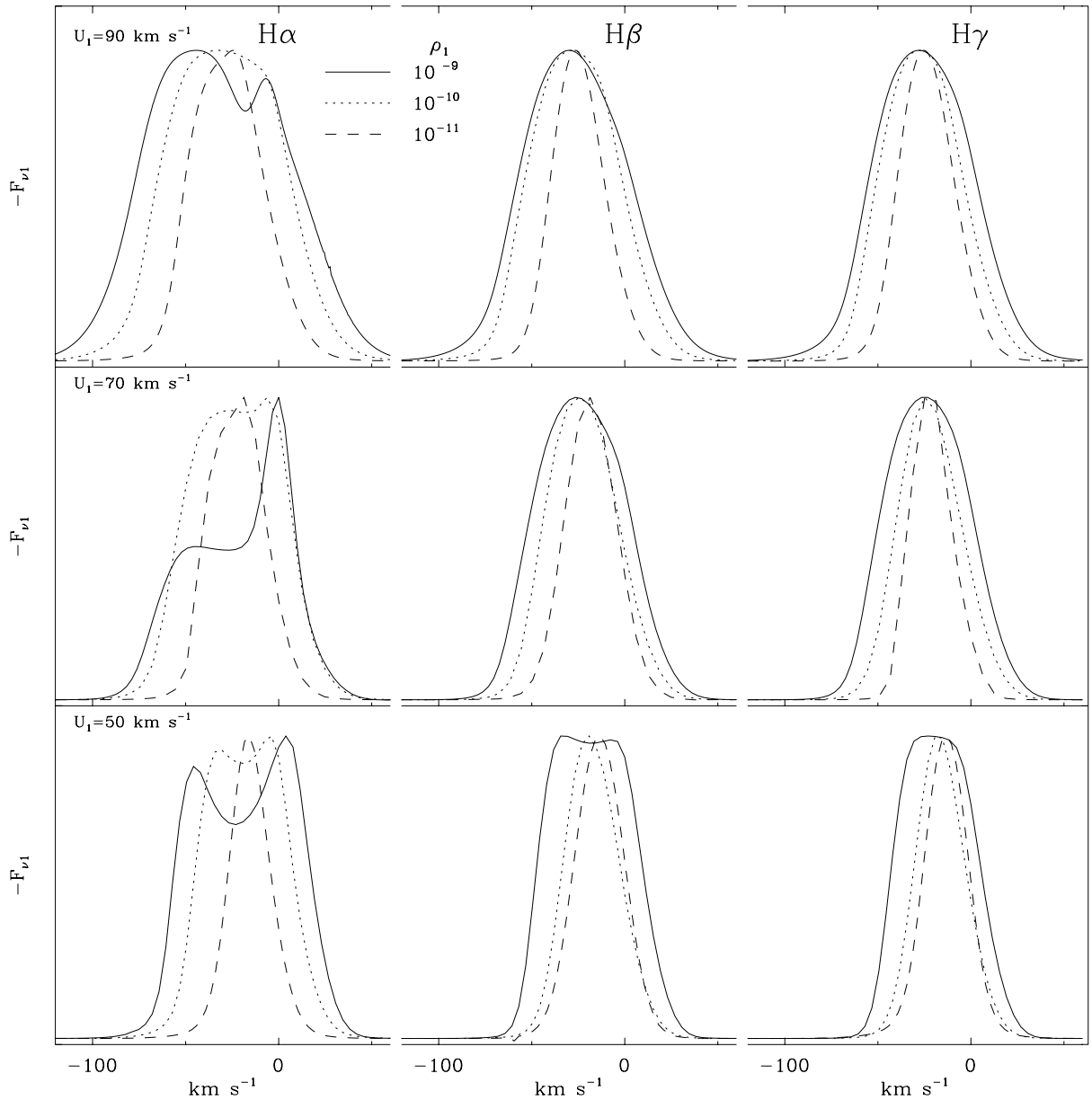

Fig. 8. The normalized monochromatic flux at the upstream face of the slab $F_{\nu 1}$ in the Hα, Hβ and Hγ frequency intervals for shock wave models with $\rho_1 = 10^{-11}$, 10^{-10}, 10^{-9} g cm^{-3}, $T_1 = 3000$ K, $U_1 = 50$, 70, 90 km s^{-1}.

As is seen in Table 1, the Doppler shifts are roughly one third of the shock wave velocity: $\delta V \approx \frac{1}{3}U_1$. There are two reasons for this. First, most of the Balmer line radiation is emitted at the rear of the shock wave where the gas undergoes strong compression and, therefore, slows down appreciably. In the upper panel in Fig. 12 we show the plots of the postshock compression ratio ρ/ρ_1 for shock wave models with $U_1 = 70$ km s^{-1}. Filled circles in the curves indicate layers with $F_\ell(\mathrm{H}\alpha) = 0$ where the compression ratio is $\eta^* = \rho^*/\rho_1 \approx 20$ for 10^{-10} g cm^{-3} $\le \rho_1 \le 10^{-9}$ g cm^{-3} and $\eta^* \approx 63$ for $\rho_1 = 10^{-11}$ g cm^{-3}. Substituting these values of η^* into Eq. (3) we find the gas flow velocity in the layers where Balmer line radiation is formed to be: $-V^* = 36$ km s^{-1} for 10^{-10} g cm^{-3} $\le \rho_1 \le 10^{-9}$ g cm^{-3} and $-V^* = 34$ km s^{-1} for $\rho_1 = 10^{-11}$ g cm^{-3}. Thus, in the Hα emitting layer the gas flow velocity in the frame of the observer is roughly one half of the shock wave velocity. Large values of the compression ratio $\eta^* = \rho^*/\rho_1$ for $\rho_1 < 10^{-10}$ g cm^{-3} are due to the small optical thickness at the Hα central frequency and, therefore, more rapid radiative cooling of the gas.

A consequence of the rapid postshock radiative cooling is that the gas flow velocity in the Hα emitting layer almost reaches its limiting value. Indeed, the upper limit of the final postshock compression ratio is given by the approximation of the isothermal shock (15). For low ionization degrees ($x_{\mathrm{H}} \ll 1$) the sound speed is almost independent of the gas density, so that for $T_1 = 3000$ K and $U_1 = 70$ km s^{-1} we have $\rho_\infty/\rho_1 = 197$. Substituting this value of the compression ratio into Eq. (3) we obtain a lower limit of the postshock velocity in the frame of the observer of $-V_\infty = 33$ km s^{-1}, whereas the

Table 1. Doppler shifts δV, $FWHM$ line widths w and line-center optical depths τ for Hα, Hβ and Hγ frequency intervals. The columns labelled V^-, V^+, V^* give the gas flow velocity in the frame of the observer just ahead of the discontinuous jump, just behind the discontinuous jump and at the Hα emitting layer. V_∞ and η_∞ are the isothermal limits of the gas flow velocity in the frame of the observer and the compression ratio. All models were computed for $T_1 = 3000$ K.

			Hα			Hβ			Hγ							
ρ_1	U_1	M_1	δV	w	$\log\tau$	δV	w	$\log\tau$	δV	w	$\log\tau$	$-V^-$	$-V^+$	$-V^*$	$-V_\infty$	η^*	η_∞
–9	40	6.2	15	64	2.0	15	49	1.1	14	41	0.7	0	29	22	19	12	64
	50	7.8	18	70	2.4	18	54	1.5	17	47	1.0	0	37	27	24	15	101
	60	9.3	22	76	2.6	21	58	1.7	20	52	1.3	0	44	32	28	18	145
	70	10.9	25	82	2.8	24	63	1.9	23	58	1.4	1	51	36	32	19	197
	80	12.5	29	88	2.9	27	67	2.0	27	64	1.6	2	58	43	35	10	258
	90	14.0	32	94	3.0	30	72	2.1	30	69	1.7	3	64	44	36	9	327
–10	40	6.2	15	45	0.7	14	28	–0.6	13	24	–0.5	0	29	20	19	32	64
	50	7.8	18	52	1.1	17	34	0.2	16	29	–0.2	0	37	26	24	26	101
	60	9.3	20	58	1.4	20	39	0.5	19	34	0.1	0	44	32	28	17	145
	70	10.9	23	65	1.6	23	45	0.7	22	39	0.3	0	51	36	32	19	197
	80	12.5	26	72	1.8	26	50	0.9	25	44	0.5	1	58	40	35	20	258
–11	60	9.3	21	25	0.2	17	33	–1.3	16	29	–1.0	0	44	30	29	60	145
	70	10.9	23	32	0.6	19	34	–1.0	19	31	–0.5	0	51	34	33	63	197
	80	12.5	26	39	0.8	22	35	–0.6	21	33	–0.4	1	58	36	35		258

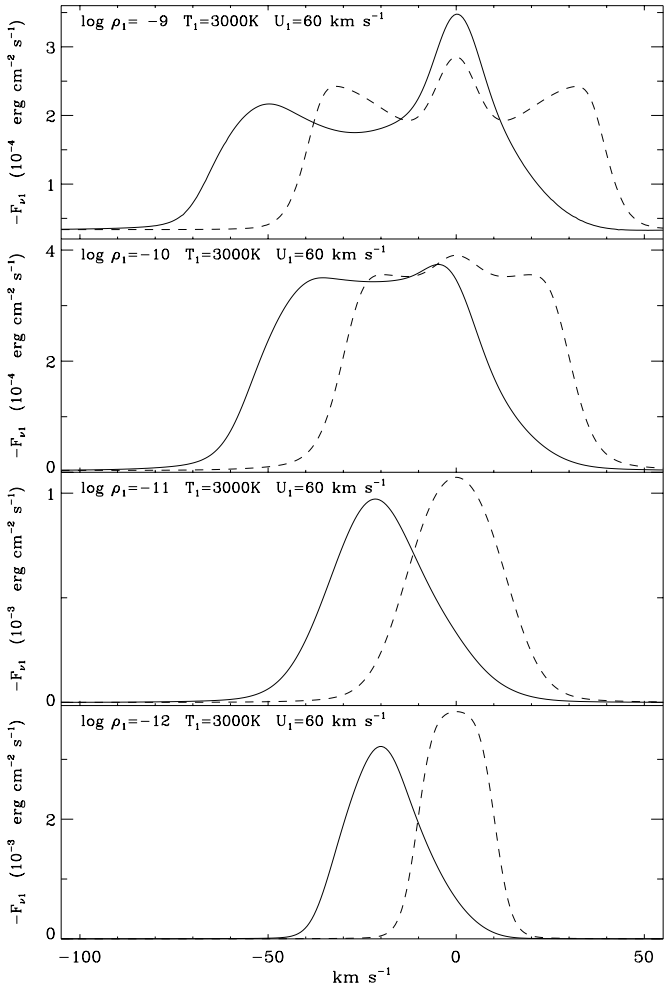

Fig. 9. The monochromatic flux emerging from the upstream face of the slab $F_{\nu 1}$ in the Hα frequency interval for the moving (solid lines) and for the static (dashed lines) medium for shock wave models with 10^{-12} g cm$^{-3} \le \rho_1 \le 10^{-9}$ g cm^{-3} and $U_1 = 60$ km s^{-1}.

gas flow velocity is $-V^* \approx 34$ km s^{-1}. Plots of the postshock gas flow velocity in the frame of the observer are shown in the lower panel in Fig. 12. However, the ratio of the Doppler shift to the gas flow velocity is $\delta V/V^* \approx 0.7$, i.e. the low gas flow velocity in the hydrogen recombination zone does not account for the small values of the Doppler shifts.

The second reason for the difference between δV and V^* is that the radiation field produced by the shock wave is characterized by an anisotropy typical for slab geometry. In Fig. 13 we show the polar diagrams of the specific intensity $I_\nu(\mu)$ for three points of the Hα frequency interval with displacements from the line center of $\delta V = 0$, 20 and 30 km s^{-1}. For the sake of simplicity the polar diagrams represent the solution of the static transfer equation, and the specific intensity $I_\nu(\mu)$ is expressed in units of the mean intensity J_ν. The radius vector connecting the origin with the point of the curve is proportional to $I_\nu(\mu)$, whereas the angle between the radius vector and the horizontal axis is the directional angle $\theta = \cos^{-1}(\mu)$. Polar diagrams in the upper and lower panels of Fig. 13 correspond to layers of the hydrogen recombination zone with $F_R < 0$ ($x_H = 0.99$) and $F_R > 0$ ($x_H = 0.27$), respectively. For the model represented in Fig. 13 the condition $F(\mathrm{H}\alpha) = 0$ is fulfilled at $x_H = 0.87$.

For the isotropic radiation field the polar diagram is the circle of unit radius shown in Fig. 13 by dashed lines. Deviations from an isotropic radiation field are quite small near the line center ($\delta V \lesssim 10$ km s^{-1}) but rapidly increase for $\delta V \gtrsim 20$ km s^{-1}. Thus, in calculating the monochromatic flux

$$F_\nu = \frac{1}{2}\int_0^1 I_\nu(\mu)\mu \mathrm{d}\mu \qquad (16)$$

we have a larger contribution of rays with $\mu \neq \pm 1$ for $\delta V \gtrsim 20$ km s^{-1} characterized by smaller values of the projection of the velocity vector onto the normal.

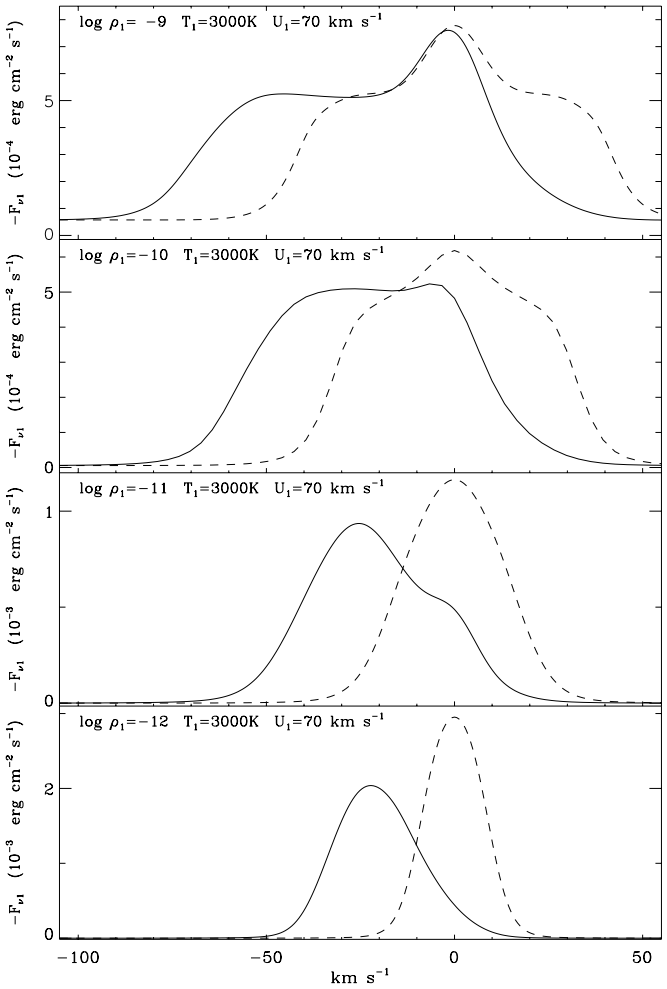

Fig. 10. The same as in Fig. 9 for shock wave models with U_1 = 70 km s^{-1}.

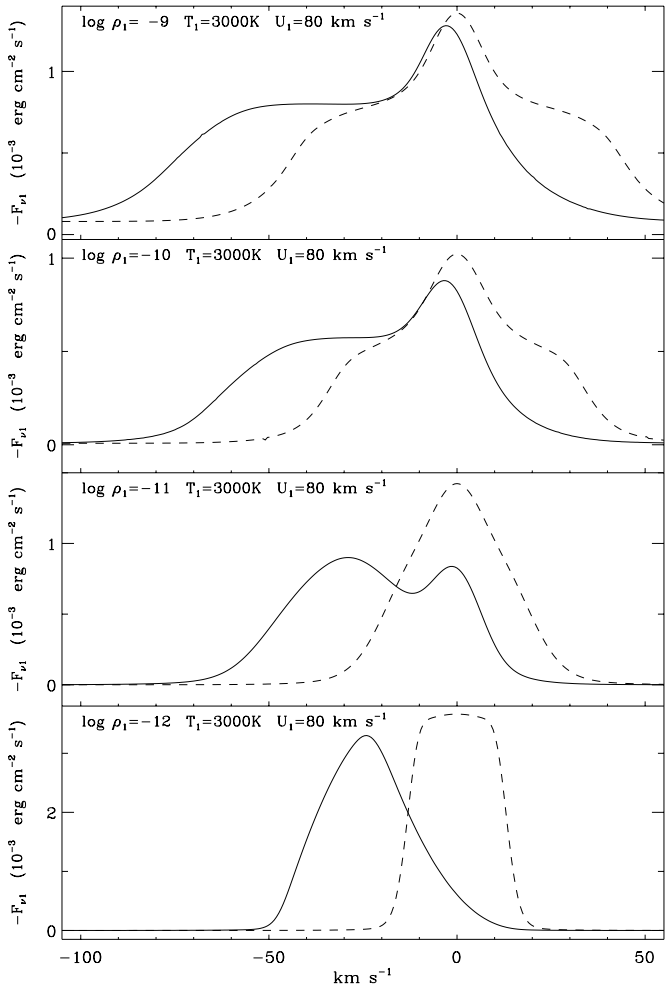

Fig. 11. The same as in Fig. 9 for shock wave models with U_1 = 80 km s^{-1}.

6. Discussion

In our attempts to solve the transfer equation for the shock wave structure in the co-moving frame we encountered a severe difficulty because of the numerical instability arising at the velocity discontinuity. In the present study this difficulty could be circumvented because the role of the radiation field in spectral lines is quite small in comparison with that of the continuum. According to our estimates the Doppler shifts in the hydrogen lines do not affect perceptibly either the structure or the radiative losses of the shock wave. In particular, the emergent flux integrated over the line frequency interval was found to be the same within $\lesssim$1% for both the static and the moving medium. This allowed us to leave out the effects of the Doppler shifts from the global iteration procedure and to solve the transfer equation in the frame of the observer only in the final iteration.

The most remarkable result of our study is that the shock wave models show the double emission structure in the Hα and Hβ profiles of the emergent radiation flux which is well known from high resolution high signal-to-noise ratio spectroscopy. We showed that the redward emission feature results from the narrow layer just ahead of the discontinuous jump within which the growth of collisional ionization is accompanied by photodeexcitation onto the second atomic level. The contribution of preshock photodeexcitation decreases with decreasing density of the ambient gas, therefore the double emission feature can be considered as a tool for diagnostics of stellar atmospheres with propagating shock waves. Here one should bear in mind, however, that in the framework of our model the unpertubed gas is at rest with respect to the observer, whereas in pulsating stars the gas ahead of the shock wave falls down onto the star with velocity in the range of one to a few dozen km s^{-1}. Thus, the preshock emission feature in Hα and Hβ profiles should be observed as a redshifted component.

Another important conclusion is that the velocity inferred from Doppler shifts of Balmer lines is roughly one-third of the shock wave velocity: $\delta V \approx \frac{1}{3}U_1$. This is due to the fact that the gas layers emitting the Balmer line radiation are located at the rear of the shock wave in the hydrogen recombination zone where the velocity in the frame of the observer is roughly one half of the shock wave velocity: $-V^* \approx \frac{1}{2}U_1$. The ratio of the Doppler shift to the gas flow velocity of $\delta V/V^* \approx 0.7$ results from the small optical thickness of the shock wave model and the anisotropy of the radiation field produced by the shock wave.

Hα is the broadest emission line with $FWHM$ comparable to the velocity of the shock wave U_1. This, as well as the

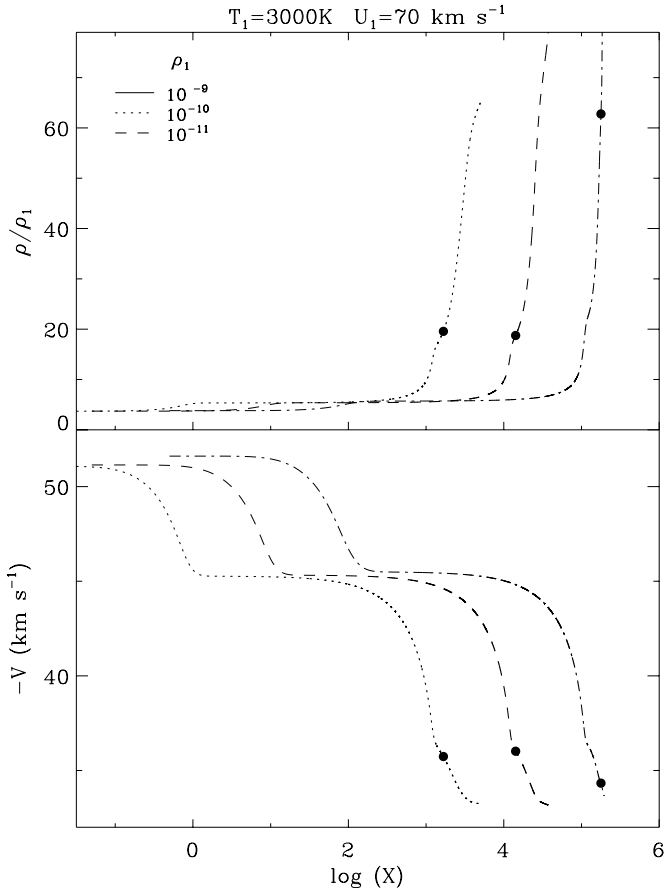

Fig. 12. The postshock compression ratio (*upper panel*) and the postshock gas flow velocity in the frame of the observer (*lower panel*) in shock waves with $U_1 = 70$ km s^{-1}. Solid lines: $\rho_1 = 10^{-9}$ g cm^{-3}; dotted lines: $\rho_1 = 10^{-10}$ g cm^{-3}, dashed lines: $\rho_1 = 10^{-11}$ g cm^{-3}. Filled circles indicate the layers of the formation of Balmer line radiation.

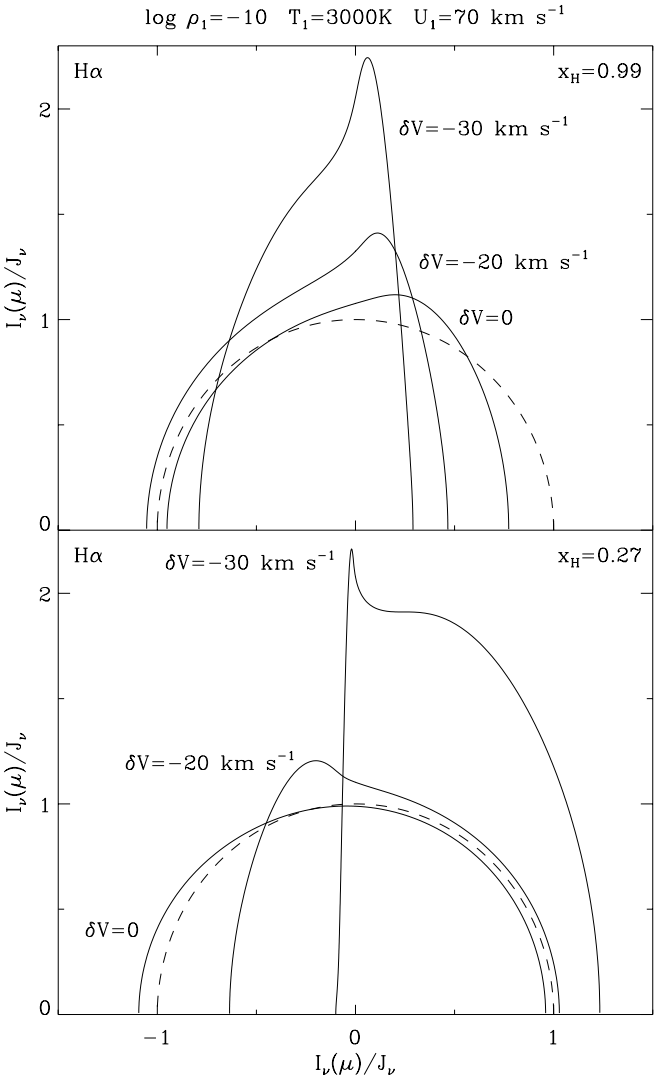

Fig. 13. Polar diagrams of the normalized specific intensity $I_\nu(\mu)$ in the frequency interval of the Hα line in the hydrogen recombination zone. *Upper panel*: layers with $F_\nu < 0$, *lower panel*: layers with $F_\nu > 0$. Plots of $I_\nu(\mu)/J_\nu$ represent the static solution of the transfer equation. The values of ΔV give the distance from the line-center frequency ν_0 expressed in units of km s^{-1}. Dashed line: the polar diagram of the isotropic radiation field.

significant contribution from the preshock photodeexcitation zone make this emission line less appropriate for inferring the velocity of the shock wave from observationally measured Doppler shifts. However the width of the emission profile is proportional to the temperature of the hydrogen atoms behind the discontinuous jump T_a^+ which is related to the shock wave velocity U_1 via the Rankine-Hugoniot relations. Thus, the width of the Balmer line is a function of two general quantities: the shock wave velocity U_1 and the ambient gas density ρ_1. In particular, the $FWHM$ of Hα decreases by a factor of two with decreasing gas density within 10^{-9} g cm^{-3} $\le \rho_1 \le$ 10^{-12} g cm^{-3}.

Though our results are consistent with the observations, there is a number of other parameters that determine the propagation of the shock wave in the atmospheres of pulsating stars. In particular, our model is confined to a flat finite slab and therefore does not take into account the cool hydrogen gas of the outer stellar atmosphere above the propagating shock wave. Thus, we cannot exclude the role of absorption in the formation of the double emission structure in Balmer lines. The presence of such absorption in emission profiles observed in RV Tau and W Vir stars was pointed out, for example, by Lèbre & Gillet (1991, 1992).

Acknowledgements. The work of Y.A.F. was done under the auspices of the Aix-Marseille I University, NATO and the Russian National Program "Astronomy" (item 1102).

References

Abt, A., & Hardie, R. H. 1960, ApJ, 131, 155
Abt, H. A. 1954, ApJS, 1, 63
Aggarwal, K., Berrington, K., Burke, P., Kingston, A., & Pathak, A. 1991, J. Phys. B, 24, 1385
Bidelman, W. P., & Ratcliffe, A. E. 1954, PASP, 66, 255
Callaway, J. 1994, ADNDT, 57, 9

Fadeyev, Y. A., & Gillet, D. 1998, A&A, 333, 687 (Paper I)
Fadeyev, Y. A., & Gillet, D. 2000, A&A, 354, 349 (Paper II)
Fadeyev, Y. A., & Gillet, D. 2001, A&A, 368, 901 (Paper III)
Fadeyev, Y. A., Le Coroller, H., & Gillet, D. 2002, A&A, 392, 735 (Paper IV)
Fox, M. W., Wood, P. R., & Dopita, M. A. 1984, ApJ, 286, 337
Gillet, D. 1988, A&A, 192, 206
Gorbatskii, V. G. 1961, SvA, 5, 192
Hutchinson, J. L., Lillie, C. F., & Hill, S. J. 1975, AJ, 80, 1044
Joy, A. H. 1947, ApJ, 106, 288
Joy, A. H. 1954, ApJS, 1, 39
Kraft, R. P., Camp, D. C., & Hughes, W. T. 1959, ApJ, 130, 90
Lèbre, A., & Gillet, D. 1991, A&A, 246, 490
Lèbre, A., & Gillet, D. 1992, A&A, 255, 221
Lennon, D. J., Brown, P. J. F., Dufton, P. L., & Lynas-Gray, A. E. 1986, MNRAS, 222, 719
Mihalas, D. 1978, Stellar atmospheres, 2nd edition (San Francisco: W. H. Freeman and Co.), 650
Mihalas, D. 1980, ApJ, 238, 1042
Mihalas, D., Kunasz, P. B., & Hummer, D. G. 1975, ApJ, 202, 465
Preston, G. W. 1962, ApJ, 136, 866
Preston, G. W. 1964, ARA&A, 2, 23
Richter, H., & Wood, P. R. 2001, A&A, 369, 1027
Rybicki, G. B., & Hummer, D. G. 1991, A&A, 245, 171
Scholz, T. T., Walters, H. R. J., Burke, P. J., & Scott, M. P. 1990, MNRAS, 242, 692
Wallerstein, G. 1959, ApJ, 130, 560
Willson, L. A. 1976, ApJ, 205, 172
Woodsworth, A. W. 1995, ApJ, 444, 396